Urban Climate 63 (2025) 102581

Contents lists available at ScienceDirect

Urban Climate

journal homepage: www.elsevier.com/locate/uclim

Introducing evaporating water channels in urban canyons: Assessment of ventilation and thermal effects through Large-Eddy Simulation

Bidesh Sengupta *, Marco Pancaldi, Silvana Di Sabatino, Carlo Cintolesi

Department of Physics and Astronomy "Augusto Righi", University of Bologna, via Irnerio 46, 40126, Bologna, Italy

ARTICLE INFO

Keywords:
Nature-based solutions
Urban blue spaces
Water evaporation
OpenFOAM
Large-Eddy simulations

ABSTRACT

Cities are particularly vulnerable to extreme weather events such as heat waves or high summer temperatures, which greatly impact public health and well-being. Climate change is expected to intensify these events and blue Nature-Based Solutions (NBS), such as water channels, have the potential to effectively mitigate temperatures and regulate the urban microclimate, but their impact on urban canyon ventilation and thermal comfort is not well understood yet. This study employs Large-Eddy Simulations (LES) with a water evaporation and heat exchange model to investigate how water channels influence airflow dynamics and temperature in a simplified urban canyon. Two configurations with a warm and cold water channel in a mixing convection regime for a Richardson number of $Ri = 3.4$, have been studied and compared to the neutral case without channel. Results show that the introduction of a water channel increases the average in-canyon turbulent kinetic energy, where addthe warm channel case showed a 61% increase compared to the cold channel case. Warm channels increase vertical mixing and buoyancy-driven turbulence, enhancing mass and momentum exchange with the atmosphere without a substantial increase in-canyon temperature. In both cases, the estimation of human comfort indices shows that the presence of water channels does not deteriorate the thermal comfort within the canyon. These findings suggest that water channels can effectively mitigate high temperatures in urban canyons, lowering the average temperature in the canyon by 1.6% (0.3%) in cold (warm) case compared to neutral ones. This study provides further evidence of the potential of blue NBS to enhance urban climate resilience.

1. Introduction

Heat waves and high temperatures have become more frequent and intense worldwide and are projected to continue worsening due to climate change (Masson-Delmotte et al., 2021; Perkins-Kirkpatrick and Lewis, 2020). Over the last two decades, Europe has experienced several major heat waves, with significant events occurring in 2003, 2010, and most recently in 2021. The 2021 heat wave was particularly notable, as it was the longest since 1950. This heat wave provides a glimpse into the potential future impacts of climate change, illustrating the increasing frequency and intensity of such extreme weather conditions. The combined effects of climate change and increasing urbanization have severe implications for human health and well-being (Watts et al., 2021; Antoniou et al., 2024); specifically, more frequent and intense heatwaves, with hotter days and warmer nights, will exacerbate the Urban Heat Island (UHI) impact on public health. The summer of 2022 also saw concerning levels of heat-related excess mortality

* Corresponding author.
E-mail address: bidesh.sengupta@unibo.it (B. Sengupta).

https://doi.org/10.1016/j.uclim.2025.102581
Received 5 March 2025; Received in revised form 31 July 2025; Accepted 10 August 2025
Available online 10 September 2025

in Europe, while 2023 has been recorded as the hottest year globally, underscoring the escalating risks associated with rising global temperatures (Klimiuk et al., 2024; Perkins-Kirkpatrick et al., 2024). South European countries, like Italy, are especially prone to extreme temperatures and heat waves have been increasing in intensity. From 1991 to 2023, data shows a national average increase of almost 2.5 heat wave days per decade, with some regions experiencing up to 4 additional days per decade (Settanta et al., 2024). This trend highlights the rapidly changing summer climate in South Europe and the urgent need for adaptation measures to mitigate the health risks associated with extreme heat.

Temperature extremes are particularly pronounced in urban areas, which generally exhibit higher temperatures than surrounding rural regions, a phenomenon known as the UHI (Howard, 1833; Lauwaet et al., 2024; Mashhoodi and Unceta, 2024), and is the most documented phenomenon of climate change in cities (Santamouris, 2015). Factors like dense infrastructure, limited vegetation, and heat generation by human activities worsen this effect, underscoring the need for strategic urban planning to investigate and adapt to future climate scenarios (Elmarakby and Elkadi, 2024; Tiwari et al., 2021). The UHI effect can be compared to a bubble of warm air over a city, which causes a local increase in urban temperature compared to the surrounding rural areas. This phenomenon is primarily caused by the high thermal conductivity of urban materials, such as concrete and asphalt, which absorb and retain heat more effectively than natural landscapes. The dense arrangement of buildings further exacerbates this effect by reducing wind ventilation airflow and vertical air transport, thereby trapping heat at street level. Additionally, the lack of natural shading elements, like trees, and the scarcity of green or blue spaces in urban environments contribute to higher temperatures, particularly during the night, as these elements play a crucial role in cooling the air (by evapotranspiration and water evaporation) and reducing heat absorption from solar radiation.

To mitigate the effects of UHI and adapt to the challenges posed by climate change, in the last decades NBS have emerged as a promising tool. NBS are actions inspired by, supported by, or modeled after nature that can help to mitigate climate change effects while enhancing citizens' well-being (Frantzeskaki et al., 2019; Girardin et al., 2021; Debele et al., 2023). They can be categorized into different types: green NBS such as city parks, avenue and roadside trees, and green roofs; blue NBS consists of water channels, urban lakes, ponds, and rivers; gray NBS which are hybrid infrastructures incorporating both natural elements and classical engineering solutions. While a large body of literature has focused on the impact of green NBS on urban microclimates (Shashua-Bar and Hoffman, 2000; Upmanis et al., 1998; Gunawardena et al., 2017; Smith and Levermore, 2008) and also diurnal variations in background wind and surface heating (Chen et al., 2025), the role of blue NBS, such as water bodies and channels, has been comparatively underexplored. However, blue NBS can play a crucial role in regulating urban microclimates by promoting vertical transport of heat and air through processes like evaporation, which helps reduce temperatures (Ampatzidis et al., 2023, 2024). Despite these potential benefits, there can be some unexpected side effects, such as increased humidity levels and reduction of thermal comfort, that need to be addressed, and their overall effectiveness in different urban contexts still requires further investigation.

Although studies have demonstrated cooling effects from water evaporation in urban areas (Grimmond and Oke, 1991), research on microclimate impacts around river corridors, particularly outside tropical regions, remains limited. Notable examples include Seoul's river daylighting project, which reduced urban temperatures (Kim et al., 2008), and studies in Nanjing, China (Huang et al., 2008), and Hiroshima, Japan, showing cooling effects up to 5°C near rivers (Murakawa et al., 1991). Ampatzidis et al. (2023, 2024) found that cooler waterbodies reduce street temperatures, while warmer ones have localized effects and revealed that larger water bodies enhance pollutant dispersion and cooling, whereas smaller or warmer ones may increase pedestrian-level heat and humidity. Further work by Ampatzidis et al. (2022) validated their solver with wind tunnel experiments, capturing evaporation effects in both forced- and mixed-convection scenarios under neutral atmospheric conditions. In forced convection, waterbodies had little impact on flow, while in mixed convection, cooler waterbodies weakened the main vortex, enhancing temperature and vapor spread. Warmer waterbodies disrupted skimming flow, aiding heat and pollutant removal. Cintolesi et al. (2021a) used LES to study urban canyons, finding that heated facades promote convective flows, improving pollutant removal and reducing urban canopy drag. These studies highlight rivers' cooling potential and suggest further analysis of urban forms for microclimate improvement. Syafii et al. (2017) found that larger water surfaces provide more significant cooling. Sun and Chen (Sun and Chen, 2012) showed that while larger water bodies offer stronger cooling, several smaller bodies of the same area have greater benefits. Theeuwes et al. (2013) confirmed this, noting larger blue spaces cool their surroundings effectively, while smaller ones influence broader areas. Despite this, there remains a limited understanding of blue spaces' thermal and dynamic interactions with urban environments (Gunawardena et al., 2017; Ampatzidis and Kershaw, 2020).

The development of computational fluid dynamics techniques has advanced the ability to study airflow dynamics and heat transfer mechanisms within urban environments, enabling more precise analyses of how blue NBS can influence local microclimates. Early studies relied on Reynolds-Averaged Navier–Stokes (RANS) simulations, which are computationally efficient but limited in capturing unsteady and turbulent flows. In contrast, LES offers higher accuracy by resolving larger turbulent eddies and modeling smaller sub-grid scales, making it more effective for studying transient phenomena and detailed urban flow structures. Although LES requires higher computational resources, its ability to reproduce three-dimensional, time-varying flows makes it ideal for analyzing complex urban environments. Studies like that one of Liu and Barth (Liu and Barth, 2002) and Walton and Cheng (Walton and Cheng, 2002) demonstrated LES's superior capability to capture turbulence and flow behavior compared to RANS, while the studies by Michioka et al. (2011, 2014) highlighted the advantage of using LES for understanding intricate urban dynamics.

Most research has yet to fully explore how water bodies affect air circulation within urban canyons, especially considering the evaporation process: the dynamic interactions between water bodies and urban environments under different thermal conditions remain largely under-researched. The present study addresses these gaps by employing LES to investigate how blue spaces influence the overall air dynamics and thermal behavior in a simplified urban canyon geometry, focusing on the role of evaporation. It

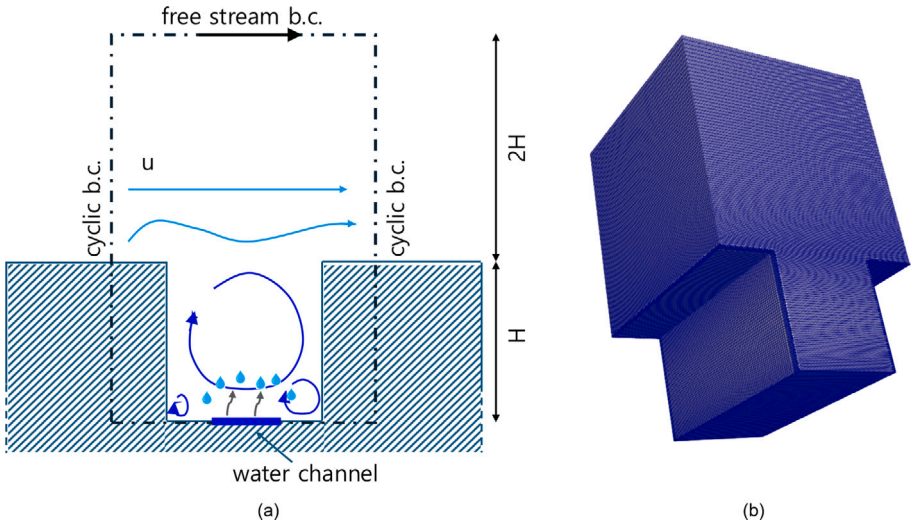

Fig. 1. (a) Schematic diagram of the problem and (b) fluid domain mesh. The canyon has an aspect ratio of $H/W = 1$, with height H and width W, where the water channel is located at the bottom of the canyon from $0.65 < x/H < 1.35$, with a constant temperature difference $\Delta T_w = T_w - T_0 = \pm 2.5$ K.

examines both cooler and warmer water channels inside a square urban canyon at the street level, under different mixed convection regimes, offering insights into the potential impact of blue spaces on urban microclimates.

The novelty of this research lies in its contribution to the understanding of blue NBS and their impact on urban microclimates. In particular, there are three points worth highlighting: (a) The study employs an in-house solver to simulate the processes of evaporation, heat exchange, and turbulence, providing detailed insights into how water channels influence convection, airflow, humidity, and heat dispersion in urban environments, contributing to enhanced urban climate resilience; (b) By utilizing LES in a simplified urban canyon configuration, the present work assesses the effects of water channels on airflow, temperature variations, and humidity, offering a more comprehensive assessment of how these features can regulate thermal comfort and improve ventilation, bridging between fundamental fluid dynamics and practical applications; (c) To the best of the authors' knowledge, this work represents one of the first attempts to assess the impact of water channels on both ventilation and thermal comfort in urban environments, providing insights for urban planners to design more climate-resilient cities.

The article is structured as follows: Section 2 describes the problem and outlines the simulation approach, including the specific environmental and physical parameters considered. Section 3 details the governing equations and computational setup, with a focus on the numerical methodologies employed. The subsequent Sections 4 and 5, present the validation of the simulation against experimental data, followed by the analysis of results within the urban canyon. Section 6 discusses the broader effects of the urban microclimate based on comfort indices. Finally, Section 7 reports the conclusions.

2. Problem description and simulation approach

The numerical investigations were conducted on a simplified configuration composed by an infinite array of two-dimensional square urban canyons. The case geometries are illustrated in Fig. 1a, which also shows the computational domain marked by dashed lines. The canyon with height H and width W, has an aspect ratio of $H/W = 1$, and the computational domain extends $2H \times 2H \times 3H$ in the streamwise (x), spanwise (y) and vertical (z) directions. The origin of the coordinate system is at the intersection of the horizontal line at street level and the vertical line through the start of the computational domain. A vertical domain height of $3H$ is considered sufficient, as vertical profiles show convergence near the top boundary with negligible variation across all cases. This suggests that unresolved outer-layer structures have minimal influence on the flow field. Previous studies indicate that while outer-scale eddies may influence pollutant removal in open environments, their effect on street canyon dispersion is less significant in quasi-steady cross-canyon flows, especially for configurations with an aspect ratio $A/R = 1$ (Michioka et al., 2011; Chew et al., 2018). The wind moves along the x-direction, perpendicular to the canyon axis, with an averaged reference velocity U_0 and temperature T_0. Reference velocity and temperature are defined, respectively, as the average of the streamwise velocity component and temperature over the top boundary of the computational domain. At the bottom of the canyon, there is a water channel located in the middle of the street at $0.65 < x/H < 1.35$, as shown in blue in Fig. 1a. The water channel is isothermal, with a constant temperature difference $\Delta T_w = T_w - T_0$ higher or lower than the ambient temperature, where T_w is the temperature of the water channel. Two cases are analyzed: in the cold-channel case, the water channel has $\Delta T_w = -2.5$ K, while in the hot-channel case, the water channel has $\Delta T_w = +2.5$ K.

3. Simulation methodology

3.1. Governing equations

The wind flow is described by the incompressible Navier–Stokes equations, using the Boussinesq approximation for the buoyancy force with the contribution of both temperature gradient and vapor concentration. The governing equations read as follows:

$$\frac{\partial u_i}{\partial x_i} = 0 \tag{1}$$

$$\frac{\partial u_i}{\partial t} + u_j \frac{\partial u_i}{\partial x_j} = -\frac{1}{\rho_0}\frac{\partial p}{\partial x_i} + \nu \frac{\partial^2 u_i}{\partial x_j \partial x_j} - b\delta_{i3} \tag{2}$$

$$b = g\frac{\rho}{\rho_0} = g\left(1 - \beta_T \Delta T - \beta_\omega \Delta\omega\right) \tag{3}$$

where u_i are the air velocity components, x_i are the Cartesian coordinate, t is time, p is the pressure, ν is the molecular kinematic viscosity, b is the buoyancy force modulus, ρ is the density which is a linear function of difference of temperature $\Delta T = T - T_0$ and vapor concentration $\Delta\omega = \omega - \omega_0$, with T and ω as the temperature and water vapor concentration, ρ_0 is the reference density, g is the gravitational acceleration, β_T and β_ω are the thermal and vapor expansion coefficient, and ω_0 is the saturated water vapor concentration at water channel temperature.

The vapor concentration ω is defined as the ratio between the mass of vapor m_v and the sum of the masses of vapor and dry air m_a:

$$\omega = \frac{m_v}{m_a + m_v} \tag{4}$$

The advection–diffusion equation for temperature and vapor concentration are:

$$\frac{\partial T}{\partial t} + u_j \frac{\partial T}{\partial x_j} = \alpha_T \frac{\partial^2 T}{\partial x_j \partial x_j} + -\frac{1}{\rho c_p}\frac{\partial}{\partial x_i} q_i \tag{5}$$

$$\frac{\partial \omega}{\partial t} + u_j \frac{\partial \omega}{\partial x_j} = \alpha_\omega \frac{\partial^2 \omega}{\partial x_j \partial x_j} \tag{6}$$

where α_T and α_ω are the coefficients of diffusion for T and ω, and q_i is the heat flux due to the phase change of water. The heat flux vector is given by $q_i = \rho^* L_h \mathbf{U}_{\omega,i}$ where $\rho^* = \rho_a + \rho_v$, ρ_a and ρ_w are the densities of air and water, L_h is the latent heat of vaporization.

The velocity of evaporation or condensation is modeled as (Petronio, 2010; Welty et al., 2001):

$$\mathbf{U}_\omega = -\frac{\alpha_\omega}{1 - \omega_T}\left(\left.\frac{d\omega}{dn}\right|_\Gamma\right)\hat{n} \tag{7}$$

where the subscript Γ indicates the quantities evaluated at the solid–fluid interface, and $\hat{n}$ is the unit normal vector through the surface of the water. Here, α_ω is based on a semi-impermeable film model (Petronio, 2010), and it is utilized to determine U_ω, which is essentially the mass-transfer rate per unit interface determined by vapor and air densities and the saturation conditions. The computed interfacial evaporation velocity $\mathbf{U}_\omega$, defined in Eq. (7), is applied as a normal mass flux boundary condition at the water surface. Specifically, it determines the net vapor flux across the air–water interface and is imposed as a Neumann-type flux condition for the vapor concentration equation (Eq. (6)). This approach ensures that the local vapor gradient at the interface consistently drives the phase change rate. The detailed derivation, equations and empirical values are presented by Cintolesi et al. (2016, 2017).

3.2. Large-eddy simulation approach

To numerically solve the governing equations, the LES approach is adopted (see e.g. Sagaut (Sagaut, 2005) and Piomelli (Piomelli, 1997)). An implicit filter is applied to Eqs. (1)–(3), as well as to the air temperature and vapor concentration Eqs. (5), (6). This results in the appearance of the following Sub-Grid Scale (SGS) additional terms:

$$\frac{\partial}{\partial x_i}\tau_{ij} = \frac{\partial}{\partial x_i}(u_i u_j - \overline{u_i}\ \overline{u_j}) \quad \text{(SGS stress tensor)} \tag{8}$$

$$\frac{\partial}{\partial x_i} h_i = \frac{\partial}{\partial x_i}(T u_i - \overline{T}\overline{u_i}) \quad \text{(SGS heat flux)} \tag{9}$$

$$\frac{\partial}{\partial x_i}\lambda_i = \frac{\partial}{\partial x_i}(\omega u_i - \overline{\omega}\ \overline{u_i}) \quad \text{(SGS vapor flux)} \tag{10}$$

where the overbar denotes the (spatially) filtered quantities. The momentum equations are closed by using the Smagorisnky turbulence model with the Van Driest wall function. The anisotropic part of the SGS stress tensor reads:

$$\tau_{ij} - \frac{\delta_{ij}}{3}\tau_{kk} = -2\nu_{sgs} S_{ij}, \tag{11}$$

where $\nu_{sgs} = c_s^2 \overline{\Delta}^2 |\overline{S_{ij}}|$ is the SGS viscosity and c_s is the Smagorinsky constant, $S_{ij} = 0.5\left(\partial\overline{u_i}/\partial x_j + \partial\overline{u_j}/\partial x_i\right)$ represents the strain rate tensor.

Table 1
Thermodynamic and fluid dynamic parameters used in the Large-Eddy Simulation (LES) of the urban street canyon.

β_T	3.3×10^{-3}	[1/K]	β_ω	0.63	–
T_0	298.15	[K]	ν	1.568×10^{-5}	[m^2/s]
Pr_t	0.7	–	Sc_t	0.7	–
ρ	1.165	[kg/m^3]	g	9.81	[m/s^2]

The temperature and vapor SGS turbulent fluxes are evaluated through the similarity theory and expressed as:

$$h_i = -\alpha_{T,sgs} \frac{\partial \overline{T}}{\partial x_i}, \quad \lambda_i = -\alpha_{\omega,sgs} \frac{\partial \overline{\omega}}{\partial x_i}, \tag{12}$$

where $\alpha_{T,sgs}$ denotes SGS thermal diffusivity and can be expressed as $\alpha_{T,sgs} = \nu_{sgs}/Pr_t$, where $Pr_t = 0.7$ is the turbulent Prandt number, $\alpha_{\omega,sgs}$ indicates SGS vapor diffusivity and can be computed as $\alpha_{\omega,sgs} = \nu_{sgs}/Sc_t$, where $Sc_t = 0.477$ is the turbulent Schmidt number. Detailed mathematical formulations of this model can be found in Cintolesi et al. (2015), which are not included here.

3.3. Computational mesh and boundary conditions

Fig. 1b shows the computational mesh used for numerical simulations, consisting of 1,592,562 cells. The mesh is refined near the boundaries to accurately capture boundary layer effects and near-wall phenomena, ensuring high fidelity in resolving flow dynamics and thermal interactions. The cells near the solid walls are constructed in such a way as to comply with the constraint $y^+ = u_\tau y/\nu < 1$ that guarantees the direct resolution of the wall-boundary layer, where u_τ is the friction velocity.

At the top boundary, an active momentum source was applied to maintain the target mean velocity using a dynamic forcing method. This approach simulates the effect of a driving pressure gradient in shear-driven flows, while a zero value is set for concentration. Solid walls enforce a no-slip condition for velocity, and pressure is imposed with a zero-gradient condition. The boundary condition for water vapor concentration at the water channel is ω_Γ and is computed as follows:

$$\omega_\Gamma = \frac{M_v}{M_a} \frac{p_s}{p_{atm} - (1 - \frac{M_v}{M_a}) p_s}, \tag{13}$$

where $M_v = 18.02$ g/mol and $M_a = 28.97$ g/mol are the values of the molar mass of air and water vapor respectively, and the saturation pressure (p_s) is evaluated by:

$$p_s = 611.85 \exp\left(\frac{17.502\ (T - 273.15)}{240.9 + (T - 273.15)}\right), \tag{14}$$

with p_{atm} is the atmospheric pressure. The production of vapor by evaporation is given by the vapor diffusion from the water surface. The process is governed by the gradient from the vapor at the water surface (Eq. (13)) and the vapor content near the surface. For the remaining solid boundaries, a zero-gradient condition is imposed. Temperature boundary conditions include constant values at various boundaries: T_0 for the top boundary, vertical walls, and street, while the water channel is set at T_w. To isolate the thermal influence of the water channels, a fixed wall and ground temperature equal to the reference value T_0 was applied, providing a neutral thermal baseline that allows direct comparison between evaporative cooling scenarios. To simulate an infinite domain in the z-direction and maintain periodicity in the x-direction, a cyclic boundary condition is applied for all variables for all other boundaries.

The simulations were initialized with a uniform velocity field ($u_x = 0.5U_0$) and zero values for all other variables. Once a steady state was reached, the simulations were run for an additional period of 6τ to gather the statistical data, where $\tau = H/0.1U_0$ is the estimation of the characteristic time of the system, based on the velocity magnitude of the system.

3.4. Physical parameters and non-dimensional numbers

The turbulence of the airflow is characterized by the Reynolds number (Re) based on building height and is defined as $Re = U_0 H/\nu$ and is set to $Re = 2.0 \times 10^4$, which exceeds the critical value needed to ensure Reynolds number independence for fluid dynamics in square urban canyons, as established in prior studies (Michioka et al., 2011; Chew et al., 2018), where $H = 1$ m and $U_0 = 0.2$ m/s. Natural convection is characterized by the Grashof number (Gr_T), which is defined by the ratio of buoyancy forces and viscous forces as:

$$Gr_T = \frac{g \beta_T \Delta T H^3}{\nu^2} \tag{15}$$

In addition to thermal effects, water vapor concentration also contributes to buoyancy. The difference in water vapor concentration is determined based on the saturated water vapor concentration (ω_0) at the reference temperature T_0. Using this water vapor concentration difference, the Grashof number (Gr_ω) can be extended to include the effects of vapor concentration on buoyancy forces and is defined as:

$$Gr_\omega = \frac{g \beta_\omega \Delta \omega H^3}{\nu^2} \tag{16}$$

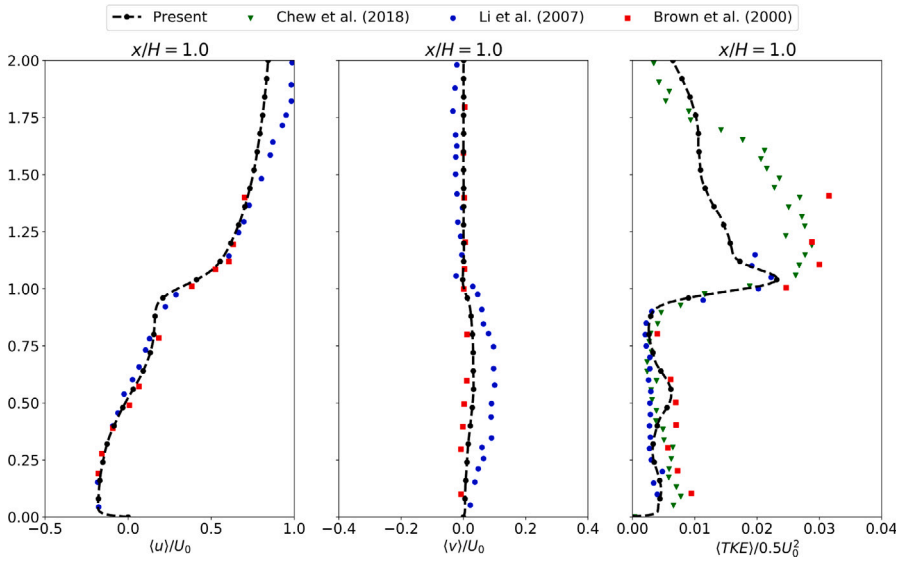

Fig. 2. Comparison of the non-dimensional mean velocity components and turbulent kinetic energy along the vertical lines: $x/H = 1.0$, with Chew et al. (2018), Li et al. (2008) and Brown et al. (2000).

In this study, a modified Richardson number (Ri_ω) formulation is used that accounts for both thermal and vapor-induced buoyancy effects. The ratio of buoyant to inertial forces is described by the Ri_ω, which can be defined from the Reynolds and Grashof numbers as:

$$Ri_\omega = \frac{Gr_T + Gr_\omega}{Re^2} \tag{17}$$

The Ri_ω define three different convection regimes: (a) Forced Convection ($Ri_\omega \ll 1$): The flow is dominated by inertial forces, and buoyancy effects are minimal, (b) Free Convection ($Ri_\omega \gg 1$): Buoyancy forces are dominant, driving the flow, (c) Mixed Convection ($Ri_\omega \approx 1$): Both buoyancy and inertial forces significantly influence the flow. In the present simulations, the $Gr_T = 8.2 \times 10^8$ and $Gr_\omega = 5.5 \times 10^8$, leading to $Ri_\omega = 3.4$. This indicates that both inertial and buoyancy forces have comparable magnitude and both effects contribute to determining the flow dynamics. The physical parameters used in the simulations are summarized in Table 1.

3.5. Numerical set-up

The simulation is conducted using the open-source software OpenFOAM (version 6.0) (The OpenFOAM Foundation, 2018). An in-house numerical solver was developed to implement the mathematical model described previously, as documented in Cintolesi et al. (2016, 2017). The pimpleFoam code was adapted to solve temperature and water vapor concentration transport equations, incorporating an evaporation model. This modified solver has been validated by Cintolesi et al. (2016, 2017).

The time discretization is performed using an implicit Euler backward scheme, and spatial discretization is achieved with a second-order central difference scheme for most terms, excluding the scalar advective term. For the scalar advective term, the Gauss–Gamma scheme, as proposed by Jasak et al. (1999), is applied with a parameter $\gamma = 0.2$. This scheme represents a bounded variant of the central-difference approach tailored for unstructured meshes, utilizing the normalized variable diagram. The overall computational accuracy of this method is second order.

Numerical clipping is applied to the vapor concentration to prevent non-physical (negative) values, which can appear in a negligible number of cells at street level during flow development. Once the statistical steady-state regime is reached, these negative fluctuations practically disappear, and plots obtained without clipping do not show detectable discrepancies compared to those with clipping.

3.6. Validation

The simulation for the case without channel is validated against existing laboratory experiments, with first- and second-order velocity statistics compared to datasets from Brown et al. (2000), Li et al. (2008), and Chew et al. (2018). Statistics are calculated over time (across a period of 6τ) and along the spanwise direction, leveraging spatial homogeneity. For a generic variable ψ, the time–spatial average is denoted by $\langle\psi\rangle$, and the fluctuation is given by $\psi' = \psi - \langle\psi\rangle$. For conciseness, only essential validation plots are presented here, focusing on the critical agreement between simulations and experiments. A more detailed validation can be found in Cintolesi et al. (2021b), where the simulation's robustness in different conditions is extensively analyzed. The validation focuses on streamwise and spanwise velocity components and resolved turbulent kinetic energy (TKE), confirming that the simulation aligns

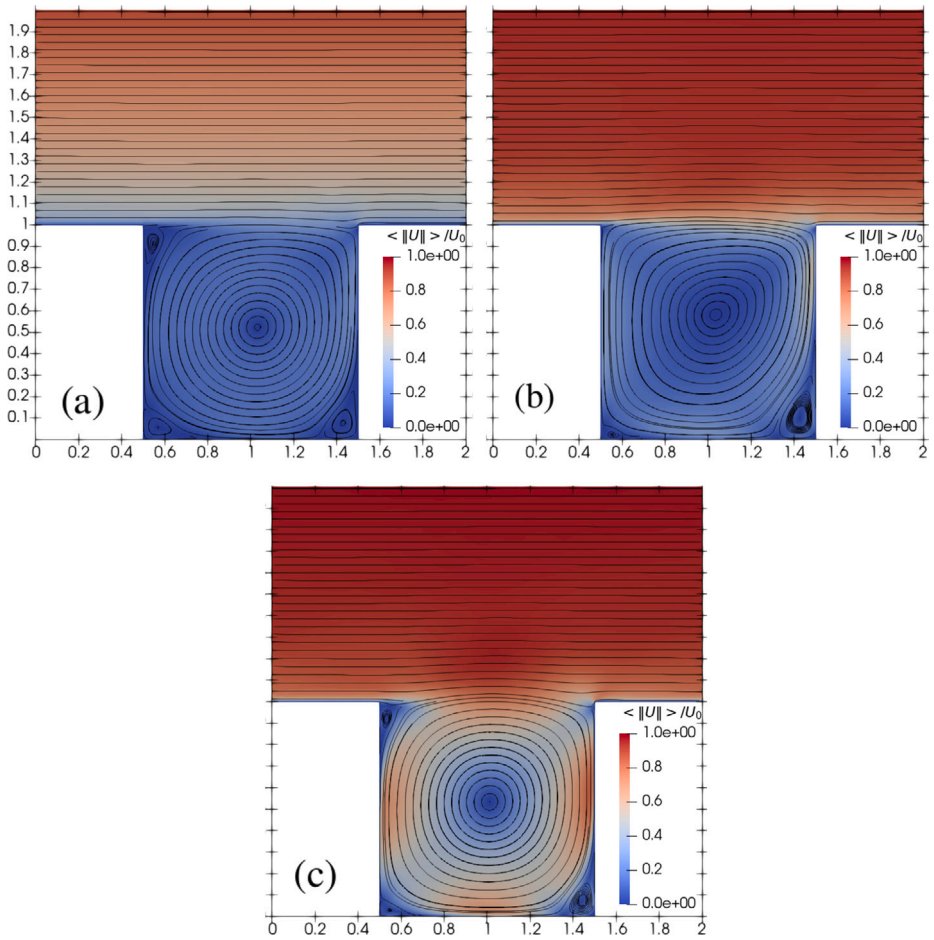

Fig. 3. Streamlines of the velocity averaged over space and time and distribution of the non-dimensional velocity averaged over space and time of (a) neutral case, (b) cold channel case, and (c) warm channel case.

well with experimental observations. Key results, such as the agreement of non-dimensional velocity components and TKE profiles, particularly at the centerline at various heights within the canyon as shown in Fig. 2, demonstrate the reliability of the numerical model in capturing turbulent flow dynamics in urban canyons. However, the TKE in the outer layer shows some discrepancy compared to the results of Brown et al. (2000) and Chew et al. (2018) (discussed in detail in Cintolesi et al. (2021b)). Minor discrepancies in vertical velocity and TKE within the canyon are consistent with previous findings and are primarily attributed to sensitivity to inflow conditions and differences among experimental setups, as noted in Cintolesi et al. (2021b), which do not significantly impact the overall validity.

4. Results

The simulation was conducted for three distinct cases: (a) a neutral case without a water channel, (b) a cold channel case where the water channel temperature is $\Delta T_w = -2.5$ K, and (c) a warm channel case where the water channel temperature is $\Delta T_w = 2.5$ K. The computational domain (Fig. 1b) is divided into four regions: the pedestrian layer ($0 < z/H < 0.15$), the middle layer ($0.15 < z/H < 0.85$), the mixing interface ($0.85 < z/H < 1.15$), and the outer layer ($z/H > 1.15$). This division reflects the distinct physical characteristics and flow dynamics within each region. The pedestrian layer represents the zone closest to the ground, where human activity takes place and airflow is heavily influenced by the presence of buildings and obstacles, making it relevant for thermal comfort studies. The middle layer is characterized by recirculating flows and is dominated by the primary vortex created by the interaction between the buildings and the ambient wind. The mixing interface, located near the rooftop level, marks the transition between the recirculating flow inside the canyon and the free-stream flow above, where strong shear and mixing occur. The outer layer represents the free-stream flow region above the urban canyon, where the airflow is less influenced by the buildings and approaches undisturbed atmospheric conditions.

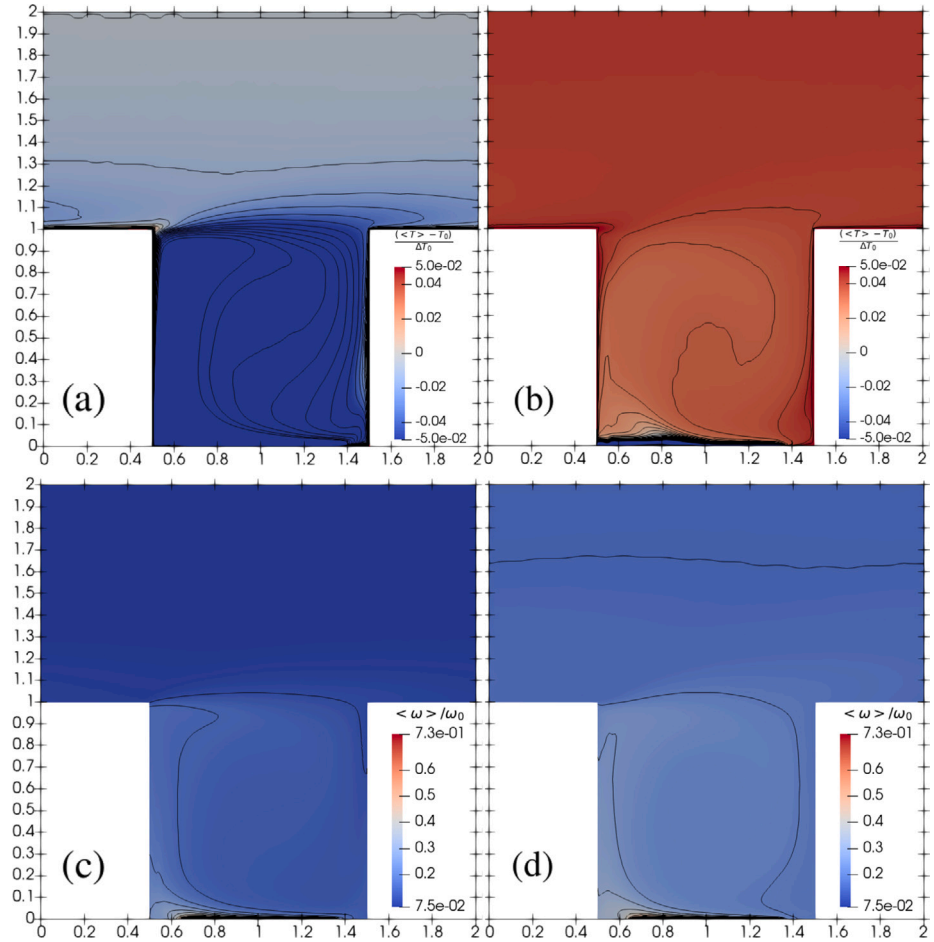

Fig. 4. Distribution of the non-dimensional temperature averaged over space and time of (a) cold channel case, (b) warm channel case (ΔT_0 = 2.5 K) and distribution of the non-dimensional water vapor concentration averaged over space and time of (c) cold channel case, (d) warm channel case.

4.1. Mean canyon dynamics

Fig. 3 shows the streamlines and the velocity averaged over space and time for the urban canyon in the three scenarios. In the neutral case, the flow exhibits the typical characteristics of urban canyon dynamics: inside the canyon, a clockwise-rotating primary vortex forms, located centrally inside the canyon. The extent of this primary vortex forms almost a straight line at the rooftop level, z/H = 1.0, with the core of the vortex situated at the canyon center. Additionally, two smaller corner vortices are present in the pedestrian layer, one near each vertical wall. Another vortex is observed at the mixing interface, adjacent to the upstream wall, which results from sharp horizontal shear generated by the ambient air at the rooftop level. The velocity profile in the outer layer exhibits a logarithmic profile, as seen in Fig. 5a.

In the cold channel case, the air in the pedestrian layer interacts with the water channel and is transported toward the upstream isothermal vertical wall by the primary vortex. As it moves along the wall, it gains momentum, leading to an acceleration that enhances the interaction between the near-wall airflow and the free-stream air at the mixing interface. This results in increased velocity near the rooftop and prevents the formation of a shear layer vortex. When the flow reaches the downstream isothermal vertical wall, changes in momentum further accelerate the adjacent air. The interaction between descending flow from the primary vortex and the upward-moving air near the downstream wall causes an expansion of the corner vortex in the pedestrian layer compared to the neutral case.

In the warm channel case, the interaction between the air and the water channel influences the flow transport mechanisms. The motion of the air is affected by phase change and conductive effects, and moves toward the upstream isothermal vertical wall. This interaction opposes the vertical motion of the primary vortex, modifying the circulation pattern when compared to the cold channel case. The flow then interacts with the outer layer at the mixing interface, forming a shear layer vortex near the rooftop, similar to the one observed in the neutral case. Near the downstream wall, the flow dynamics remain comparable to the neutral scenario, resulting in a corner vortex in the pedestrian layer that closely resembles that of the neutral case.

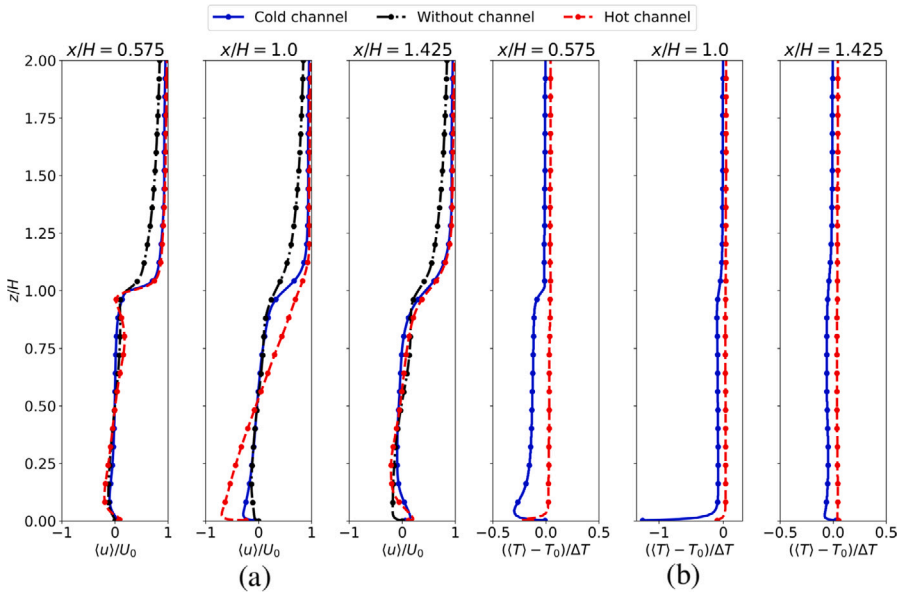

Fig. 5. Non-dimensional (a) velocity component in the streamwise direction and (b) temperature ($\Delta T = 2.5$ K) averaged over space and time at three locations: $x/H = 0.575, 1.0$ and 1.425.

Fig. 4a and 4b present the non-dimensional temperature distribution, averaged in space and time, for cold channel and warm channel cases. In the cold channel case, the temperature inside the canyon is lower than the free-stream temperature. As the air comes in contact with the cold water channel in the pedestrian layer, its temperature decreases primarily due to the phase change of water. However, given the low thermal conductivity of air, the phase change becomes the dominant factor in this temperature reduction, as shown in Fig. 5b. Near the upstream wall, the air temperature decreases at the bottom and gradually increases with height. In the mixing interface, the air interacts with the free-stream, leading to a high-temperature gradient, before reaching a value close to the free-stream temperature due to limited vertical mixing, as seen in Fig. 6d. At the center of the canyon ($x/H = 1.0$) and near the downstream wall ($x/H = 1.425$), the temperature is relatively uniform due to enhanced turbulence and mixing inside the canyon, as depicted in Fig. 6c and Fig. 8b. Due to reduced vertical mixing with the outer layer, cold air remains largely confined within the canyon, as shown in Fig. 6d.

In the warm channel case, as air comes into contact with the water in the channel, evaporation causes a temperature decrease in the vicinity of the channel in the pedestrian layer. The resulting cooler layer of air is transported throughout the canyon by the primary vortex, showing a slight decrease of temperature around 15% compared to the outer layer, as depicted in Fig. 4b. However, the overall temperature within the canyon remains uniform, with a gradual transition from the inside of the canyon to the outer layer, as seen in Fig. 5b, due to enhanced mixing and transport, as shown in Fig. 6f and Fig. 8c. While the temperature in the outer layer becomes nearly constant in both cases, the cold channel scenario maintains lower temperatures compared to the warm channel, as expected. The average canyon temperature is reduced by 1.6% and 0.3% in the cold channel and warm channel cases, respectively, compared to the neutral case.

Fig. 4c and 4d present the non-dimensional water vapor concentration distribution, averaged in space and time, for the cold channel and warm channel case, respectively. In the cold channel case, the air near the water channel exhibits the highest water vapor concentration at the pedestrian level. The water vapor is transported by the primary vortex throughout the canyon, with its concentration gradually decreasing with height due to mixing, as shown in Fig. 6c and 6d. Near the upstream wall at the mixing interface, the concentration gradient is high due to limited mixing in that region, while the gradient is lower at the center and near the downstream wall, indicating stronger mixing at those locations, as illustrated in Fig. 6d.

In the warm channel case, the vapor concentration near the channel is higher compared to the cold channel case. Similar to the cold channel scenario, the water vapor is distributed throughout the canyon by the primary vortex, as seen in Fig. 3c, with enhanced mixing observed in Fig. 6f. At the mixing interface, the concentration gradient is lower than in the cold channel case due to increased mixing and transport at the interface, which is evident from Fig. 6e and 8c. Interestingly, despite the higher water vapor concentration inside the canyon in the warm channel case, the removal rate of water vapor through the mixing interface is higher due to the stronger mixing and transport observed at this location.

4.2. Turbulence inside the canyon

The resolved Reynolds stress components $u'u'$ and $v'v'$ represent the variance of velocity fluctuations in the streamwise and vertical directions, respectively. Fig. 6 shows the non-dimensional resolved streamwise and vertical Reynolds stress (RS) distribution,

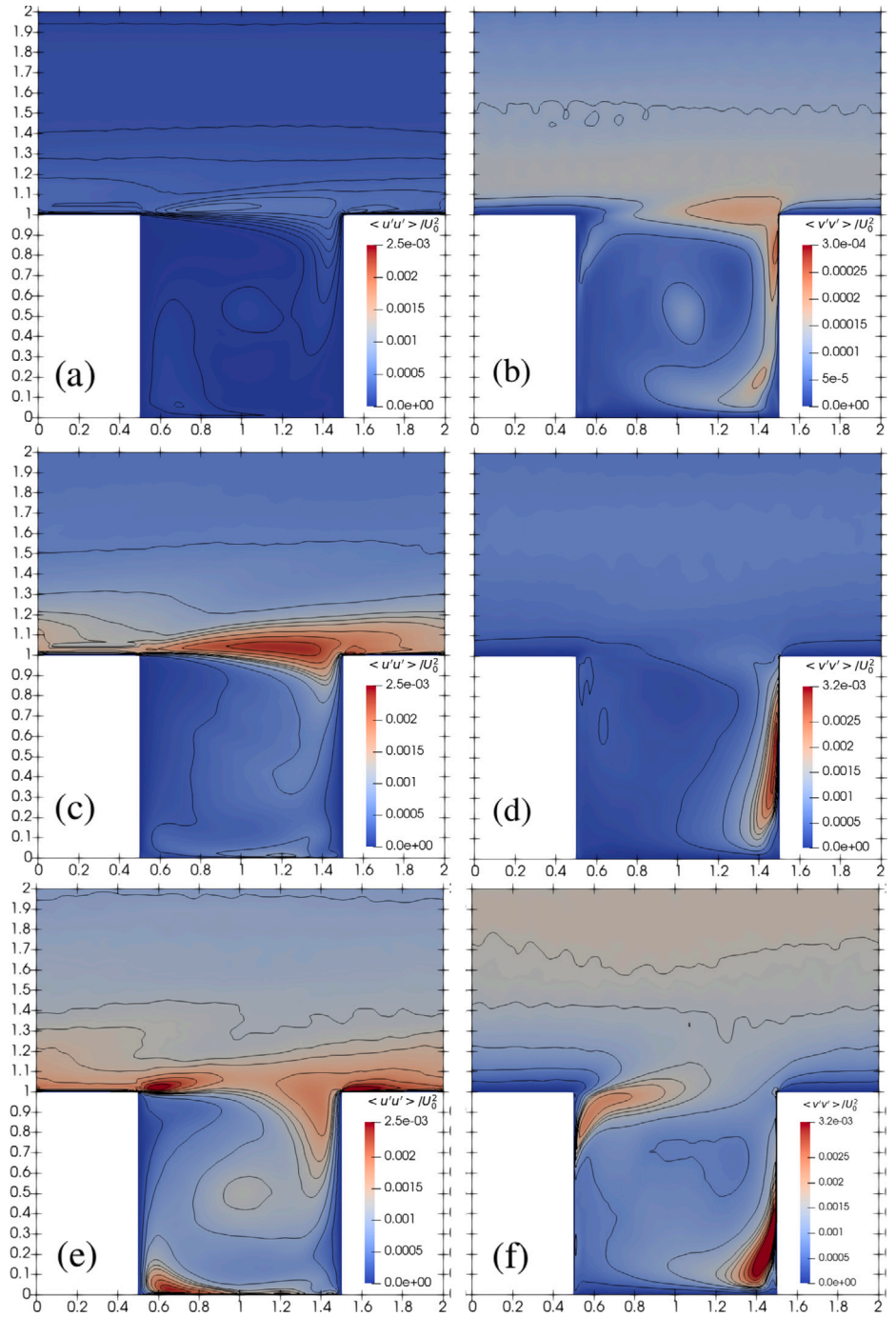

Fig. 6. Distribution of the non-dimensional resolved Reynolds stress in streamwise (left column) and vertical (right column) direction averaged over space and time for (a) neutral, (c) cold channel, and (e) warm channel in the streamwise direction, and (b) neutral, (d) cold channel, and (f) warm channel in the vertical direction.

averaged in space and time, for the three cases. In the neutral case, the streamwise and spanwise RS within the canyon exhibit low values, with a local maximum appearing at the mixing interface, as depicted in Fig. 6a and 6b when compared with cold channel and warm channel cases, and moderate RS observed in the outer layer.

In the cold channel case, moderate RS is found in both the streamwise and vertical directions inside the canyon. The mixing interface exhibits high streamwise RS ($\langle u'u' \rangle$), while a local maximum is observed near the downstream vertical wall for vertical RS ($\langle v'v' \rangle$), as seen in Fig.s 6c, 6d and is further confirmed by the line plot in Fig. 7b at $x/H = 1.425$. Moderate RS values are

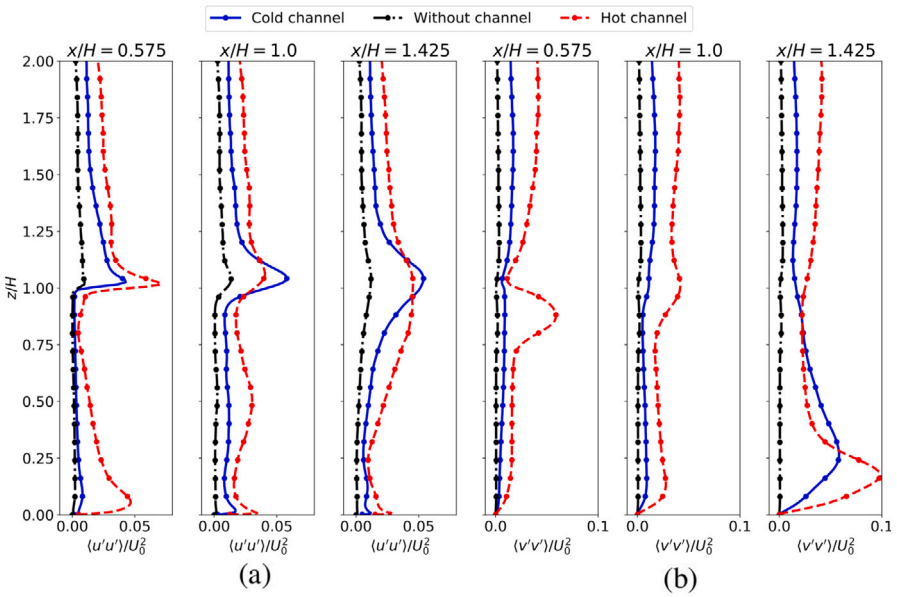

Fig. 7. Non-dimensional resolved Reynolds stress in the (a) streamwise direction and (b) vertical direction averaged over space and time at three locations: $x/H = 0.575, 1.0$ and 1.425.

also present in the outer layer. In the warm channel case, moderate RS levels are observed in both directions inside the canyon, as depicted in Fig. 6e, 6f. A local maximum is detected near the upstream vertical wall in the mixing interface for streamwise RS, with high values extending across the interface, and another local maximum is found on the left side of the pedestrian layer. In the vertical direction, two local maxima are identified: one near the upper side of the upstream wall and another near the lower side of the downstream wall. The magnitude of RS in both directions for the neutral case is at least twice lower and, at most, up to ten times lower compared to the water channel cases, as shown in Fig. 7.

Overall, the neutral case exhibits the lowest RS at any location, as it lacks the thermal buoyancy effects present in the warm and cold channel cases. In the cold channel case, higher streamwise RS is observed at the mixing interface due to buoyancy-driven acceleration of cold air from the water channel toward warmer walls, creating sharp thermal gradients and increased turbulent mixing. The warm channel case shows significantly higher vertical RS compared to both other cases, except near the downstream wall in the middle layer, where the cold channel has a higher RS. This is because the buoyant rising air in the warm channel intensifies vertical turbulent motions, creating strong shear layers. In contrast, the cold air descending near the downstream wall in the cold channel generates more pronounced vertical shear due to the temperature differential, leading to increased RS in that region. The introduction of a water channel leads to a significant rise in the in-canyon turbulent kinetic energy. The warm channel case, in particular, shows a 61% increase compared to the cold channel case.

Fig. 8 shows the non-dimensional turbulent kinematic momentum fluxes (KMF) averaged in space and time ($\langle u'v' \rangle$) for three cases, and following the turbulent-viscosity hypothesis, turbulent KMF may be modeled by the gradients of the mean velocity (Pope, 2001). It reads:

$$\langle u'v' \rangle \approx -\nu_{SGS} \left(\frac{\partial \langle u \rangle}{\partial x} + \frac{\partial \langle v \rangle}{\partial y} \right) \tag{18}$$

In the neutral case, KMF values are almost zero, except at the interface and a small area above it, indicating limited vertical turbulent exchange. In the cold channel case, positive KMF values on the right side of the pedestrian layer signify the descent-flow region (Fig. 8b, near the downstream wall in the pedestrian layer), while the negative peak at the interface reflects enhanced mixing. This indicates that vertical turbulent transport is driven by cold air from the channel interacting with warmer air, resulting in increased mixing at the interface. In the warm channel case, the larger positive KMF values in the pedestrian layer indicate an expanded descent-flow region, where warm air from the channel accelerates downward. The significantly larger negative peak at the interface, almost double that of the cold channel case, implies a much stronger vertical turbulent exchange. This can be explained by the intensified buoyancy forces in the warm channel, which promote upward and downward mixing, increasing vertical momentum transfer and enhancing turbulent mixing.

Fig. 9 displays the non-dimensional turbulent kinematic temperature fluxes (KTF) in the streamwise and vertical direction for warm and cold channel cases. These fluxes can be interpreted using the flux-gradient hypothesis:

$$\langle T'u_i' \rangle \simeq -\kappa_i \frac{\partial T}{\partial x_i}, \tag{19}$$

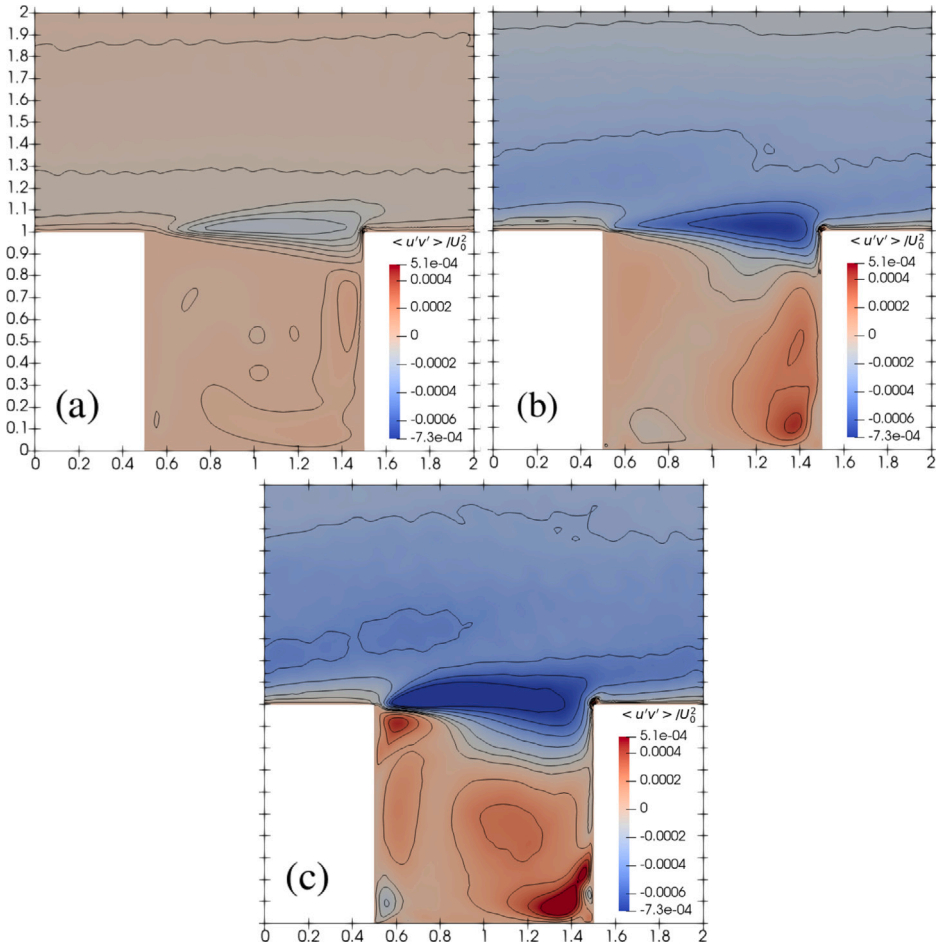

Fig. 8. Distribution of the non-dimensional turbulent kinematic momentum flux averaged over space and time for (a) neutral, (b) cold channel, and (c) warm channel.

where κ_i is a positive constant, implying that negative (positive) turbulent flux increases (decreases) temperature diffusion along the i-direction. In the cold channel case, negative values of both streamwise (Fig. 9a) and vertical (Fig. 9c) turbulent temperature fluxes (TTF) are observed near the water channel, indicating enhanced temperature diffusion in both directions, as also shown in Fig. 10. Positive streamwise TTF at the mixing interface near the upstream wall reduces temperature diffusion, leading to a high-temperature gradient in that area (Fig. 4a). However, streamwise TTF decreases further downstream in the mixing interface, resulting in a lower temperature gradient in that region (Fig. 4a). The negative vertical TTF in the mixing interface indicates high-temperature diffusion, with the values decreasing in the downstream direction, as shown in Fig. 9c. This contributes to an increased diffusion of temperature in the downstream direction within the mixing interface, which is evident in the temperature distribution in Fig. 4a. In the warm channel case, the temperature near the water channel decreases due to water change of phase. The primary vortex transports air from the channel, likely causing the observed negative streamwise TTF near the channel (Fig. 9b). The positive vertical TTF near the upstream wall in the pedestrian layer suggests reduced vertical temperature diffusion (Fig. 9d and 10b at $x/H = 0.575$). Both streamwise and vertical TTFs inside the canyon show small negative values, promoting temperature diffusion throughout the canyon, which results in a relatively uniform temperature distribution and minimal temperature gradients within the canyon, as shown in Fig. 4b.

4.3. Effect on urban micro-climate

In urban canyon environments, the assessment of human thermal comfort is crucial for understanding the impact of urban design on public health and well-being. Urban canyons, formed by buildings on either side of a street, often experience altered microclimatic conditions due to restricted airflow and enhanced heat retention. To evaluate thermal comfort within these settings, several indices can be employed. This section analyzes three commonly used indices to quantify human comfort based on meteorological parameters

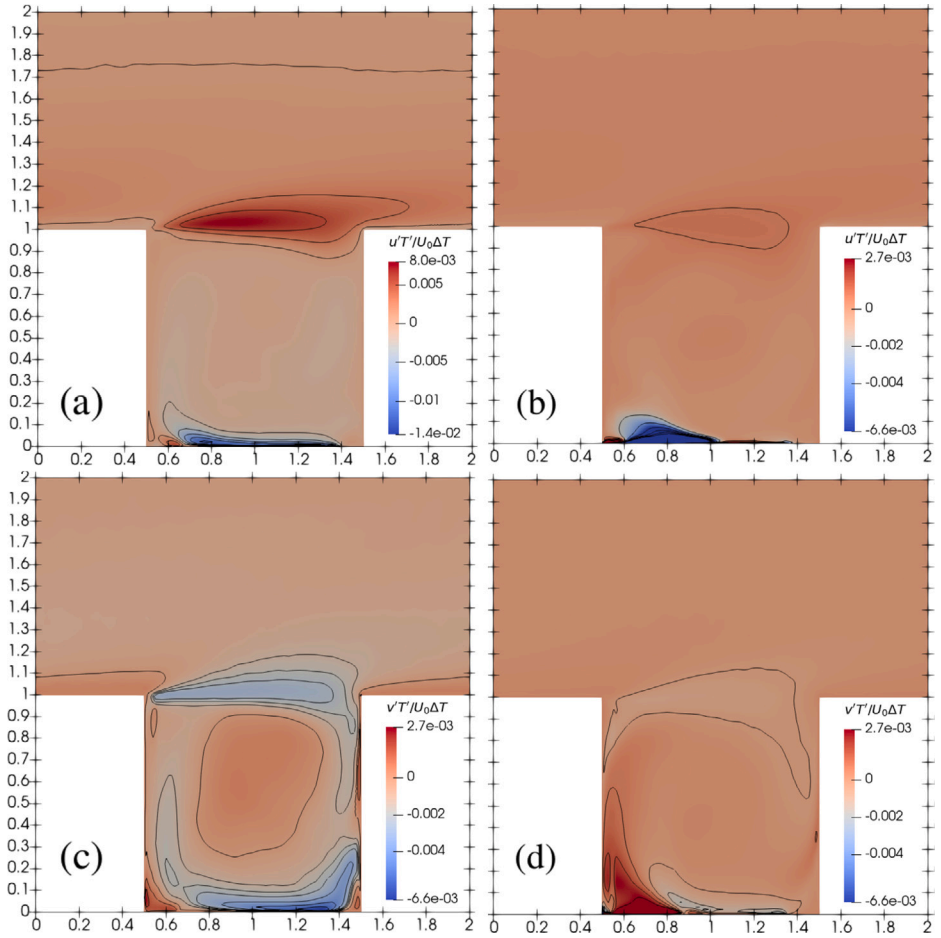

Fig. 9. Distribution of the non-dimensional turbulent temperature flux averaged over space and time for cold channel in the (a) streamwise direction and (c) vertical direction, and warm channel in the (b) streamwise direction and (d) vertical direction.

derived from urban canyon simulations. All of these are computed from the relative humidity, which is estimated as $RH = 100\,\omega/\omega_s$, where ω_s is the saturation vapor concentration given by:

$$\omega_s = \frac{M_w\ p_s}{R\ (T_C + 273.15)} \tag{20}$$

where T_C is the temperature in Celsius, $R = 8.314$ J/(mol K) is the universal gas constant. The three indices selected for the analysis of thermal comfort are: HI, Humidex and WBGT.

The HI estimates the apparent temperature, representing how hot it feels to the human body by accounting for both air temperature and humidity, with higher values indicating a greater risk of heat stress due to high humidity exacerbating the perceived temperature (Anderson et al., 2013). This is estimated as follows:

$$\begin{aligned} HI =& c_1 + c_2 T_F + c_3 RH + c_4 T_F\ RH + c_5 T_F^2 + \\ & c_6 RH^2 + c_7 T_F^2\ RH + c_8 T_F\ RH^2 + c_9 T_F^2\ RH^2, \end{aligned} \tag{21}$$

where T_F is in Fahrenheit and the empirical constants here used are reported in Table 2. The Humidex reflects perceived heat but is particularly sensitive to humidity; high Humidex values suggest severe discomfort or heat-related health risks (Rana et al., 2013). It is a function of dewpoint temperature (T_d) and reads:

$$\text{Humidex} = T_C + 0.5555\left[6.112\exp\left(\frac{17.67\ T_d}{T_d + 243.5}\right) - 10\right] \tag{22}$$

where the dewpoint temperature is calculated according to Magnus–Tetens approximation as $T_d = b\ \alpha/(a - \alpha)$, where $a = 17.27$ and $b = 237.7$ °C are model constants, while α is a function of T_C and RH:

$$\alpha(T_C, RH) = \frac{aT_C}{b + T_C} + \ln\left(\frac{RH}{100}\right). \tag{23}$$

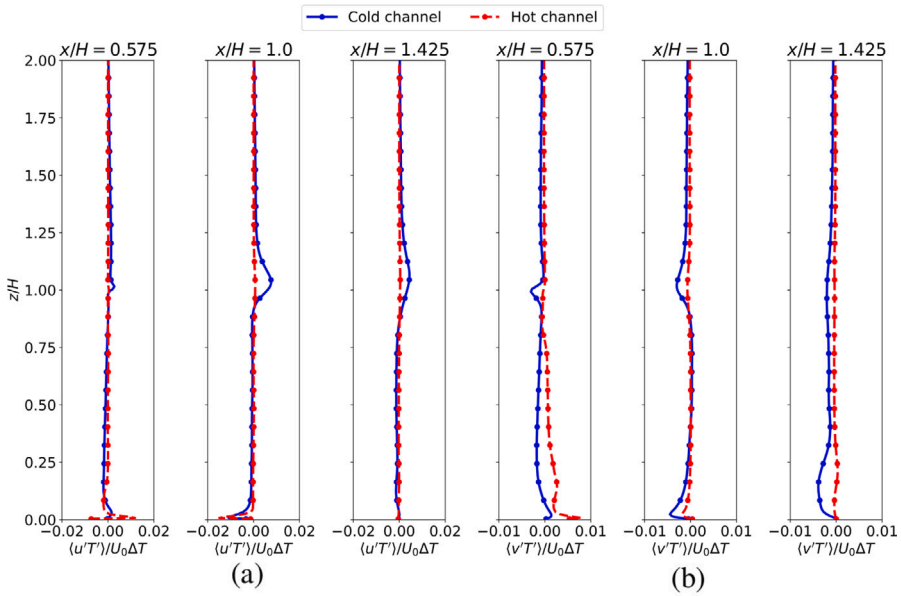

Fig. 10. Non-dimensional turbulent temperature flux in the (a) streamwise direction and (b) vertical direction averaged over space and time at three locations: $x/H = 0.575, 1.0$ and 1.425.

Table 2
Constants used in the HI equation (Eq. (21)).

c_1	16.923	c_4	−0.100254	c_7	0.000345372
c_2	0.185212	c_5	0.00941695	c_8	−0.000814971
c_3	5.37941	c_6	0.00728898	c_9	0.0000102102

The WBGT index indicates more extreme heat stress conditions, which are critical for evaluating outdoor environments in urban canyons where solar radiation can significantly affect comfort levels (Moran et al., 2001). It reads:

$$\mathrm{WBGT} = 0.7T_{wb} + 0.2T_g + 0.1T_C \tag{24}$$

where T_{wb} is the wet bulb temperature and is given by Stull's Formula as:

$$\begin{aligned} T_{wb} \approx T_C \ & \tan^{-1}(0.151977\ \sqrt{RH + 8.313659}) + \tan^{-1}(T_C + RH) \\ & - \tan^{-1}(RH - 1.676331) + 0.00391838\ RH^{3/2} \\ & \tan^{-1}(0.023101\ RH) - 4.686035, \end{aligned} \tag{25}$$

where T_g is the globe temperature. A constant globe temperature was used across all simulations to ensure consistency, and the variation in WBGT between cases reflects only the changes in air temperature and humidity due to evaporative effects. Lower values across these indices generally suggest safer, more comfortable conditions, whereas higher values imply potential heat stress.

Fig. 11 presents the human comfort indices for both cold and warm channel cases, comparing them to their respective threshold values. These thresholds define comfort zones, with values below the threshold indicating thermal comfort (green zone) and those above signifying discomfort (red zone) (National Weather Service, 2024; Rotronic Monitoring System, 2024; Forbes, 2024). 'Left' and 'Right' refer to the probe lines placed near the upstream ($x/H = 0.6$) and downstream ($x/H = 1.4$) buildings. The results show that the cold channel case exhibits a higher level of thermal comfort compare to the warm channel case across all indices, with values well within the comfort zone. The warm channel scenario leads to increased temperature and humidity but does not exceed discomfort thresholds. HI remains relatively uniform across the canyon in both cases, indicating little variation in discomfort with height. Humidex, being more sensitive to humidity, indicates greater discomfort for the warm channel due to higher evaporation rates. WBGT remains relatively uniform, with slight variations near the canyon floor. Overall, the cold channel provides better comfort as expected, while the warm channel results in lower comfort but still remains below the discomfort thresholds. A comparison between upstream (Right) and downstream (Left) locations shows that discomfort tends to be higher downstream, particularly in the warm channel scenario, likely due to differing airflow and heat exchange patterns.

These estimations emphasize the effectiveness of water channels in maintaining thermal comfort within acceptable level. Even if the freestream temperature were to increase by more than 3 °C and humidity levels were raised by 50%, it is estimated that the indices would remain within the comfort zone. This suggests that the presence of urban water channels, whether cooler or warmer than the ambient air, plays a positive role in regulating local microclimate conditions.

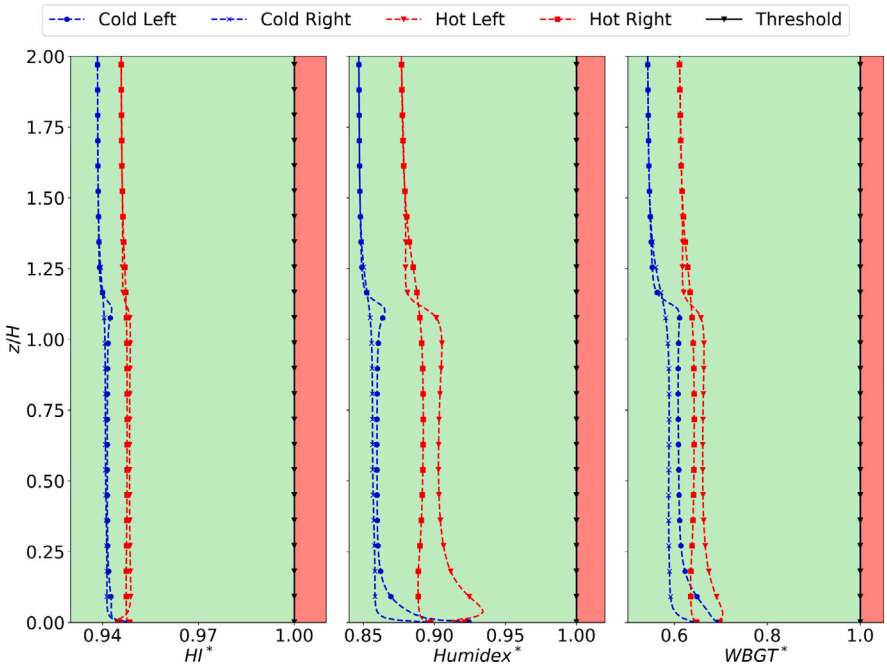

Fig. 11. Human comfort indices for different water channel temperature cases compared with threshold comfort values (black solid line). Green (Red) areas denote the comfortable (uncomfortable) zone. The indices are normalized with respect to their respective threshold values. 'Cold' and 'Hot' denote the scenarios where the water channel temperatures are lower or higher than the ambient free stream, respectively.

5. Summary and conclusions

The present study uses Large-Eddy Simulation (LES) to assess the impact of blue Nature-Based Solutions (NBS), specifically water channels, on a simplified urban canyon. The simulation approach utilizes an in-house numerical solver, particularly suitable to reproduce three-dimensional turbulent flow dynamics (including convective turbulence effects) within the canyon, together with the water evaporation and heat exchange due to water change of phase. Two selected scenarios are analyzed and compared with the baseline scenarios (no water channel): a cold and warm channel case, where the water temperature is set below and above the atmospheric free-stream temperature, respectively. Each case was analyzed across four vertical layers (pedestrian layer, middle layer, mixing interface, and outer layer) to understand the water channel influence on the overall flow dynamics, temperature distribution, turbulence, water vapor concentration, and human thermal comfort.

In the pedestrian layer, the cold channel stabilizes flow by cooling the air through water evaporation and thermal conduction, keeping the cooler air near the ground. Hence, buoyancy and vertical mixing are reduced, together with turbulence level (quantified by the velocity variances). This promotes the formation of an almost stationary region near the ground. Conversely, the warm channel introduces strong buoyancy-driven convection, which advects the humid air from the water channel into the canyon. This creates more energetic turbulent vertical mixing. In the middle layer, the cold channel inhibits the formation of corner recirculation vortices. The evaporating water cools the air, and its interaction with the warmer building facades induces near-wall buoyancy, reducing shear near the mixing interface. In contrast, the warm channel slightly warms the air, enhancing vertical motions and strengthening the primary vortex within the canyon by increasing velocity intensity and TKE. In the mixing interface (at the rooftop level), two distinct dynamics are established: in the cold-channel case, a limited vertical mixing creates a sharp temperature gradient with the free-stream air, leading to high-velocity variances in the streamwise direction. The hot-channel case exhibits a smoother temperature gradient across this interface due to more effective vertical mixing. This leads to a larger exchange of momentum and heat between the canyon and the surrounding atmosphere, which contributes to temperature diffusion. In the outer layer, the dynamics are largely unaffected by the presence of the water, but the hot-channel cases lead to an increase in temperature because of the more effective turbulent mixing and heat transport.

The vapor distribution follows a pattern similar to that of temperature. In the cold channel, vapor concentration is higher near the water surface within the pedestrian layer, where limited evaporation results in a limited concentration level. The primary vortex advects vapor throughout the canyon, but it remains more concentrated in the lower half of the canyon and near the downstream wall. Vapor accumulates within the canyon, indicating strong thermal and vapor stratification. In the warm channel, the larger evaporation from the warmer water increases the vapor concentration, which is uniformly distributed throughout the canyon due to stronger advection and mixing. The concentration gradient at the mixing interface is lower compared to the cold channel case, as buoyancy-driven turbulent mixing actively transports vapor upward and outward, resulting in a higher vapor removal rate. This

also leads to lower vapor stratification within the canyon. The rise in temperature and vapor concentration within the canyon does not significantly impact thermal comfort, with all indices remaining below discomfort thresholds, although the warm channel case exhibits slightly higher values due to enhanced evaporation, particularly affecting the pedestrian layer and the upstream facade where humid air accumulates. The cold channel reduces the average canyon temperature by 1.6%, whereas the warm channel leads to a 0.3% decrease, both relative to the neutral case. Additionally, the presence of a water channel significantly increases the average in-canyon turbulent kinetic energy, with the warm channel showing a 61% rise compared to the cold channel.

In conclusion, the present study underscore the role of blue NBS in the ventilation and thermal regulation of urban canyons. In-canyon temperature is mainly driven by the water evaporation process, which reduces temperature and does not significantly deteriorate thermal comfort indexes even in the presence of warm water. Hence, channels can play a positive role in mitigating heat extremes in cities. The impact on canyon ventilation depends on the water temperature. The presence of a warm channel can represent a nighttime period, where the water stores the heat absorbed during the day. In this case, the in-canyon circulation and turbulent exchanges with the atmosphere are fostered, resulting in better ventilation of the canyon. The presence of a cold channel can mimic a daytime configuration (under the approximation of no sun radiation), where water keeps a low temperature after the night. This results in reduced air circulation within the canyon and an area of very low velocities at the pedestrian level. Such a feature contributes to maintaining the canyon at a low temperature but reduces the overall ventilation. This may lead to undesirable effects, such as elevated pollutant concentrations in the lower part of the canyon, particularly if emission sources are present. These considerations can help urban planners with a careful installation of blue NBS, such as water channels, although the present study represents a first investigation using a simplified geometry. This work shall be extended to explore the complex physics of pollutant dispersion in more realistic urban environments.

CRediT authorship contribution statement

Bidesh Sengupta: Writing – original draft, Investigation, Formal analysis, Conceptualization. **Marco Pancaldi:** Validation, Software, Formal analysis. **Silvana Di Sabatino:** Writing – review & editing, Project administration. **Carlo Cintolesi:** Writing – review & editing, Supervision, Project administration, Conceptualization.

Declaration of competing interest

The authors declare that they have no known competing financial interests or personal relationships that could have appeared to influence the work reported in this paper.

Acknowledgments

This work received financial support under the National Recovery and Resilience Plan (NRRP), Mission 4, Component 2, Investment 1.1, Call for tender No. 104 published on 2.2.2022 by the Italian Ministry of University and Research (MUR), funded by the European Union – NextGenerationEU. Project Title *“Multi-scale investiGation of natuRe-basEd solutions for thE mitigatioN of urban heat and POLlution ISland (GREEN-POLIS)”* authorized by MUR – CUP J53D23002560001 - Grant Assignment Decree No. 20224HHCK7_001. The authors acknowledge the use of computational resources from the parallel computing cluster of the Open Physics Hub at the Department of Physics and Astronomy “Augusto Righi” at the University of Bologna (Italy).

Data availability

Data will be made available on request.

References

Ampatzidis, Petros, Cintolesi, Carlo, Kershaw, Tristan, 2023. Impact of blue space geometry on urban heat island mitigation. Climate 11 (2), 28.

Ampatzidis, Petros, Cintolesi, Carlo, Petronio, Andrea, Sabatino, Silvana Di, Kershaw, Tristan, 2022. Evaporating waterbody effects in a simplified urban neighbourhood: A rans analysis. J. Wind Eng. Ind. Aerodyn. 227, 105078.

Ampatzidis, Petros, Cintolesi, Carlo, Sabatino, Silvana Di, Kershaw, Tristan, 2024. Blue space effects on urban flow and pollution dispersion in a stable atmosphere. Urban Clim. 55, 101898.

Ampatzidis, Petros, Kershaw, Tristan, 2020. A review of the impact of blue space on the urban microclimate. Sci. Total Environ. 730, 139068.

Anderson, G. Brooke, Bell, Michelle L., Peng, Roger D., 2013. Methods to calculate the heat index as an exposure metric in environmental health research. Environ. Health Perspect. 121 (10), 1111–1119.

Antoniou, Nestoras, Montazeri, Hamid, Blocken, Bert, Neophytou, Marina, 2024. On the impact of climate change on urban microclimate, thermal comfort, and human health: multiscale numerical simulations. Build. Environ. 111690.

Brown, M., Lawson, R., DeCroix, D., Lee, R., 2000. Mean flow and turbulence measurements around a 2-d array of buildings in a wind tunnel, 11th ams appl. of air poll. In: Meteor. Conf.

Chen, Guanwen, Mei, Shuo-Jun, Hang, Jian, Li, Qingman, Wang, Xuemei, 2025. URANS simulations of urban microclimates: Validated by scaled outdoor experiments. Build. Environ. 272, 112691.

Chew, Lup.Wai., Aliabadi, Amir.A., Norford, Leslie.K., 2018. Flows across high aspect ratio street canyons: Reynolds number independence revisited. Environ. Fluid Mech. 18, 1275–1291.

Cintolesi, Carlo, Barbano, Francesco, Sabatino, Silvana Di, 2021a. Large-eddy simulation analyses of heated urban canyon facades. Energies 14 (11), 3078.

Cintolesi, Carlo, Petronio, Andrea, Armenio, Vincenzo, 2015. Armenio large eddy simulation of turbulent buoyant flow in a confined cavity with conjugate heat transfer. Phys. Fluids 27 (9).
Cintolesi, Carlo, Petronio, Andrea, Armenio, Vincenzo, 2016. Large-eddy simulation of thin film evaporation and condensation from a hot plate in enclosure: First order statistics. Int. J. Heat Mass Transfer 101, 1123–1137.
Cintolesi, Carlo, Petronio, Andrea, Armenio, Vincenzo, 2017. Large-eddy simulation of thin film evaporation and condensation from a hot plate in enclosure: Second order statistics. Int. J. Heat Mass Transfer 115, 410–423.
Cintolesi, Carlo, Pulvirenti, Beatrice, Sabatino, Silvana Di, 2021b. Large-eddy simulations of pollutant removal enhancement from urban canyons. Bound.-Layer Meteorol. 180, 79–104.
Debele, Sisay E., Leo, Laura S., Kumar, Prashant, Sahani, Jeetendra, Ommer, Joy, Bucchignani, Edoardo, Vranić, Saša, Kalas, Milan, Amirzada, Zahra, Pavlova, Irina, et al., 2023. Nature-based solutions can help reduce the impact of natural hazards: A global analysis of nbs case studies. Sci. Total Environ. 902, 165824.
Elmarakby, Esraa, Elkadi, Hisham, 2024. Impact of urban morphology on urban heat island in manchester's transit-oriented development. J. Clean. Prod. 434, 140009.
Forbes, 2024. Wet bulb globe temperature is great for heat warnings - why don't we use it ?. https://www.forbes.com/sites/marshallshepherd/2019/08/14/wet-bulb-globe-temperature-is-great-for-heat-warningswhy-dont-we-use-it/#ecd5dcdf25ba. Accessed: 2024-09-26.
Frantzeskaki, Niki, McPhearson, Timon, Collier, Marcus J., Kendal, Dave, Bulkeley, Harriet, Dumitru, Adina, Walsh, Claire, Noble, Kate, Wyk, Ernita Van, Ordóñez, Camilo, et al., 2019. Nature-based solutions for urban climate change adaptation: Linking science, policy, and practice communities for evidence-based decision-making. BioScience 69 (6), 455–466.
Girardin, Cécile A.J., Jenkins, Stuart, Seddon, Nathalie, Allen, Myles, Lewis, Simon L., Wheeler, Charlotte E., Griscom, Bronson W., Malhi, Yadvinder, 2021. Nature-based solutions can help cool the planet—if we act now.
Grimmond, Christine Susan Betham, Oke, Timothy R., 1991. An evapotranspiration-interception model for urban areas. Water Resour. Res. 27 (7), 1739–1755.
Gunawardena, Kanchane R., Wells, Martin J., Kershaw, Tristan, 2017. Utilising green and bluespace to mitigate urban heat island intensity. Sci. Total Environ. 584, 1040–1055.
Howard, Luke, 1833. The Climate of London: Deduced from Meteorological Observations Made in the Metropolis and At Various Places Around It, vol. 3, Harvey and Darton, J. and A. Arch, Longman, Hatchard, S. Highley [and] R. Hunter.
Huang, Liangmei, Zhao, Dehua, Wang, Jiazhen, Zhu, Jiyu, Li, Jianlong, 2008. Scale impacts of land cover and vegetation corridors on urban thermal behavior in nanjing, china. Theor. Appl. Climatol. 94, 241–257.
Jasak, Hrvoje, Weller, H.G., Gosman, A.D., 1999. High resolution nvd differencing scheme for arbitrarily unstructured meshes. Internat. J. Numer. Methods Fluids 31 (2), 431–449.
Kim, Y.-H., Ryoo, S.-B., Baik, J.-J., Park, I.-S., Koo, H.-J., Nam, J.-C., 2008. Does the restoration of an inner-city stream in seoul affect local thermal environment? Theor. Appl. Climatol. 92, 239–248.
Klimiuk, Tatiana, Ludwig, Patrick, Sanchez-Benitez, Antonio, Goessling, Helge F., Braesicke, Peter, Pinto, Joaquim G., 2024. The european summer heatwave 2019: A regional storyline perspective. Earth Syst. Dyn. Discuss. 2024, 1–24.
Lauwaet, Dirk, Berckmans, Julie, Hooyberghs, Hans, Wouters, Hendrik, Driesen, Guy, Lefebre, Filip, Ridder, Koen De, 2024. High resolution modelling of the urban heat island of 100 european cities. Urban Clim. 54, 101850.
Li, Xian-Xiang, Leung, Dennis Y.C., Liu, Chun-Ho, Lam, Kit Ming, 2008. Physical modeling of flow field inside urban street canyons. J. Appl. Meteorol. Clim. 47 (7), 2058–2067.
Liu, Chun-Ho, Barth, Mary C., 2002. Large-eddy simulation of flow and scalar transport in a modeled street canyon. J. Appl. Meteorol. 41 (6), 660–673.
Mashhoodi, Bardia, Unceta, Pablo Muñoz, 2024. Urban form and surface temperature inequality in 683 european cities. Sustain. Cities Soc. 113, 105690.
Masson-Delmotte, V.P., Zhai, Panmao, Pirani, S.L., Connors, C., Péan, S., Berger, N., Caud, Y., Chen, L., Goldfarb, M.I., Monteiro, Pedro M. Scheel, 2021. Ipcc, 2021: Summary for policymakers. In: Climate Change 2021: The Physical Science Basis. Contribution of Working Group I To the Sixth Assessment Report of the Intergovernmental Panel on Climate Change.
Michioka, Takenobu, Sato, Ayumu, Takimoto, Hiroshi, Kanda, Manabu, 2011. Large-eddy simulation for the mechanism of pollutant removal from a two-dimensional street canyon. Bound.-Layer Meteorol. 138, 195–213.
Michioka, Takenobu, Takimoto, Hiroshi, Sato, Ayumu, 2014. Large-eddy simulation of pollutant removal from a three-dimensional street canyon. Bound.-Layer Meteorol. 150 (2), 259–275.
Moran, Daniel S., Pandolf, Kent B., Shapiro, Y., Heled, Y., Shani, Y., Mathew, W.T., Gonzalez, R.R., 2001. An environmental stress index (esi) as a substitute for the wet bulb globe temperature (wbgt). J. Therm. Biol. 26 (4–5), 427–431.
Murakawa, Saburo, Sekine, Takeshi, Narita, Ken-Ichi, Nishina, Daisaku, 1991. Study of the effects of a river on the thermal environment in an urban area. Energy Build. 16 (3–4), 993–1001.
National Weather Service, 2024. What is the heat index?. https://www.weather.gov/ama/heatindex. (Accessed 26 September 2024).
Perkins-Kirkpatrick, Sarah, Barriopedro, David, Jha, Roshan, Wang, Lin, Mondal, Arpita, Libonati, Renata, Kornhuber, Kai, 2024. Extreme terrestrial heat in 2023. Nat. Rev. Earth Environ. 5 (4), 244–246.
Perkins-Kirkpatrick, S.E., Lewis, S.C., 2020. Increasing trends in regional heatwaves. Nat. Commun. 11 (1), 3357.
Petronio, Andrea, 2010. Numerical investigation of condensation and evaporation effects inside a tub. In: School of Environmental and Industrial Fluid Mechanics. University of Trieste.
Piomelli, U., 1997. Large-eddy and direct simulation of turbulent flows. Introduction to the Modelling of Turbulence.
Pope, Stephen B., 2001. Turbulent flows. Meas. Sci. Technol. 12 (11), 2020–2021.
Rana, Rajib, Kusy, Brano, Jurdak, Raja, Wall, Josh, Hu, Wen, 2013. Feasibility analysis of using humidex as an indoor thermal comfort predictor. Energy Build. 64, 17–25.
Rotronic Monitoring System, 2024. Umidex monitoring. https://www.rotronic.com/en/humidity_measurement-feuchtemessung-mesure_de_l_humidite/humidex-humidity-index-mr. (Accessed 26 September 2024).
Sagaut, Pierre, 2005. Large Eddy Simulation for Incompressible Flows: An Introduction. Springer Science & Business Media.
Santamouris, M., 2015. Analyzing the heat island magnitude and characteristics in one hundred asian and australian cities and regions. Sci. Total Environ. 512, 582–598.
Settanta, Giulio, Fraschetti, Piero, Lena, Francesca, Perconti, Walter, Piervitali, Emanuela, 2024. Recent Tendencies of Extreme Heat Events in Italy: From 1991 To Present Days. Technical report, Copernicus Meetings.
Shashua-Bar, Limor, Hoffman, Michael E., 2000. Vegetation as a climatic component in the design of an urban street: An empirical model for predicting the cooling effect of urban green areas with trees. Energy Build. 31 (3), 221–235.
Smith, Claire, Levermore, Geoff, 2008. Designing urban spaces and buildings to improve sustainability and quality of life in a warmer world. Energy Policy 36 (12), 4558–4562.
Sun, Ranhao, Chen, Liding, 2012. How can urban water bodies be designed for climate adaptation? Landsc. Urban Plan. 105 (1–2), 27–33.
Syafii, Nedyomukti Imam, Ichinose, Masayuki, Kumakura, Eiko, Jusuf, Steve Kardinal, Chigusa, Kohei, Wong, Nyuk Hien, 2017. Thermal environment assessment around bodies of water in urban canyons: A scale model study. Sustain. Cities Soc. 34, 79–89.
The OpenFOAM Foundation, 2018. OpenFOAM (version 6.0). http://openfoam.org. (Accessed 12 February 2025).

Theeuwes, Natalie E., Solcerova, Anna, Steeneveld, Gert J., 2013. Modeling the influence of open water surfaces on the summertime temperature and thermal comfort in the city. J. Geophys. Res.: Atmos. 118 (16), 8881–8896.
Tiwari, Arvind, Kumar, Prashant, Kalaiarasan, Gopinath, Ottosen, Thor-Bjørn, 2021. The impacts of existing and hypothetical green infrastructure scenarios on urban heat island formation. Environ. Pollut. 274, 115898.
Upmanis, Hillevi, Eliasson, Ingegärd, Lindqvist, Sven, 1998. The influence of green areas on nocturnal temperatures in a high latitude city (göteborg, sweden). Int. J. Clim.: A J. R. Meteorol. Soc. 18 (6), 681–700.
Walton, A., Cheng, A.Y.S., 2002. Large-eddy simulation of pollution dispersion in an urban street canyon—part ii: idealised canyon simulation. Atmos. Environ. 36 (22), 3615–3627.
Watts, Nick., Amann, Markus, Arnell, Nigel, Ayeb-Karlsson, Sonja, Beagley, Jessica, Belesova, Kristine, Boykoff, Maxwell, Byass, Peter, Cai, Wenjia, Campbell-Lendrum, Diarmid, et al., 2021. The 2020 report of the lancet countdown on health and climate change: Responding to converging crises. Lancet 397 (10269), 129–170.
Welty, J.R., Wicks, Ch E., Wilson, R.E., Rorrer, G., 2001. Fundamentals of mass transfer, fundamentals of momentum. Heat Mass Transf. 4, 438–442.